# Yield scaling, size hierarchy and fluctuations of observables in fragmentation of excited heavy nuclei

N. Le Neindre, E. Bonnet, J.P. Wieleczko, B. Borderie, F. Gulminelli, M.F. Rivet, R. Bougault, A. Chbihi, R. Dayras, J.D. Frankland, et al.

# Yield scaling, size hierarchy and fluctuations of observables in fragmentation of excited heavy nuclei.

N. Le Neindre [a], E. Bonnet [a], J.P. Wieleczko [b], B. Borderie [a],
F. Gulminelli [c], M.F. Rivet [a], R. Bougault [c], A. Chbihi [b],
R. Dayras [d], J.D. Frankland [b], E. Galichet [a,e], D. Guinet [f],
P. Lautesse [f], O. Lopez [c], J. Lukasik [g,h], D. Mercier [c],
J. Moisan [b,i], M. Pârlog [b,j], E. Rosato [k], R. Roy [i], C. Schwarz [g],
C. Sfienti [g], B. Tamain [c], W. Trautmann [g], A. Trzcinski [ℓ],
K. Turzo [g], E. Vient [c], M. Vigilante [k] and B. Zwieglinski [ℓ]

(INDRA and ALADIN collaborations)

[a] *Institut de Physique Nucléaire, CNRS/IN2P3, Université Paris-Sud 11, F-91406 Orsay cedex, France.*

[b] *GANIL, CEA/DSM-CNRS/IN2P3, B.P. 5027, F-14076 Caen cedex, France.*

[c] *LPC, CNRS/IN2P3, ENSICAEN, Université de Caen, F-14050 Caen cedex, France.*

[d] *CEA Saclay, DAPNIA/SPhN, Orme des Merisiers, F-91191 Gif sur Yvette cedex, France.*

[e] *Conservatoire National des Arts et Métiers, F-75141 Paris cedex 03, France.*

[f] *Institut de Physique Nucléaire, CNRS/IN2P3, Université Claude Bernard Lyon 1, F-69622 Villeurbanne cedex, France.*

[g] *Gesellschaft für Schwerionenforschung mbH, D-64291 Darmstadt, Germany.*

[h] *Institute of Nuclear Physics IFJ-PAN, PL-31342 Kraków, Poland.*

[i] *Laboratoire de Physique Nucléaire, Département de Physique, de Génie Physique et d'Optique, Université Laval, Québec, Canada G1K 7P4.*

[j] *National Institute for Physics and Nuclear Engineering, RO-76900 Bucharest-Măgurele, Romania.*

[k] *Dipartimento di Scienze Fisiche e Sezione INFN, Università di Napoli "Federico II", I80126 Napoli, Italy.*

[ℓ] *The Andrzej Soltan Institute for Nuclear Studies, PL-00681, Warsaw, Poland.*

**Abstract**

Multifragmentation properties measured with INDRA are studied for single sources

produced in Xe+Sn reactions in the incident energy range 32-50 A MeV and quasi-projectiles from Au+Au collisions at 80 A MeV. A comparison for both types of sources is presented concerning Fisher scaling, Zipf law, fragment size and fluctuation observables. A Fisher scaling is observed for all the data. The pseudo-critical energies extracted from the Fisher scaling are consistent between Xe+Sn central collisions and Au quasi-projectiles. In the latter case it also corresponds to the energy region at which fluctuations are maximal. The critical energies deduced from the Zipf analysis are higher than those from the Fisher analysis.

# 1 Introduction

From the radial dependence of the nucleon-nucleon interaction, containing both repulsive and attractive parts, the nuclear phase diagram is expected to present a first order liquid-gas phase transition and a second order phase transition at the critical point [1]. Nuclear collisions offer a large panoply of initial conditions that allow to probe the properties of excited nuclear systems and to deduce the structure of the phase diagram. It is well established that the production of many fragments is the dominant phenomenon in reactions over a range of incident energy from the Fermi energy up to relativistic energies, both in central and semi-peripheral collisions and in reactions induced by heavy ions or hadrons on heavy targets (see [2] for a recent and exhaustive review on experimental status). In the chapter "Systematics of fragment observables" of this review [3], it is mentioned that fragment production is essentially governed by excitation (dissipated) energy, dynamical effects being responsible for the observed deviations around the general behaviour. This universal phenomenology does not necessarily imply that the occurence of fragmentation has to be associated with a unique mechanism, nor that a single trajectory is systematically followed across the phase diagram.

A crucial piece of information in studies of the fragmentation process is cluster size distributions. They inform on intrinsic properties of finite excited systems such as scaling laws, size hierarchy or large fluctuations [4,5,6,7,8,9,10,11,12]. These behaviours are actively searched for in multifragmentation data since on the basis of theoretical grounds they could signal that nuclear systems have undergone a phase transition.

Extraction of a scaling law for the cluster size distribution based on Fisher

Droplet Model has been reported in a wide variety of collisions from 8 GeV/c $\pi$ and 10.2 GeV/c proton + Au to quasi-projectile (QP) events from peripheral 35 A MeV Au+Au collisions [2,13,14,15,16,17,18]. From the fitting procedure of fragment yield distributions with the Fisher ansatz, it is possible to extract the energy at which the cluster size distributions follow a power law, and the associated critical exponents. In some works, the interpretation of the observed scaling has been pushed further, claiming that thermodynamical variables, like the temperature and density of the system at the critical point can be extracted [13]. On the other hand, analyses on QP events have shown that the excitation energy corresponding to this power law is associated to a peak of abnormal fluctuation in configurational energy which rather signals a system in a coexistence region of the phase diagram [18]. Since both interpretations were derived in two different bombarding energy regimes, it is worthwhile to investigate more deeply the scaling properties of the fragment yields on new sets of data.

Based on Lattice Gas Model calculations, it was recently suggested [6] to examine a specific ordering of the cluster size, the so-called Zipf law [19]; in this case, $<Z_2> = <Z_1>/2$, $<Z_3> = <Z_1>/3$, $...,<Z_n> = <Z_1>/n$ where n is the rank of the $n^{th}$ cluster in an event having M clusters ordered by decreasing size $Z_1 > Z_M$. According to the model, such a law would be verified at or close to the critical point, see also [20]. Experimental investigations [21,22] on the disintegration of quasi-projectiles in violent $^{40}$Ar+$^{27}$Al, $^{48}$Ti and $^{58}$Ni collisions at 47 A MeV have shown that both critical behaviour and Zipf law are observed at the same excitation energy E$^*$=5-6 A MeV. Thus, the authors conclude that the Zipf law could be a reliable signature to reveal a critical point. However, it has been recently pointed out [23] that the Zipf law would be a direct consequence of a power law in the yield distribution and would not bring more information than the observation of a power law. Since the conclusions of [21,22] were strongly supported by the fact that a large variety of observables shows a maximal fluctuation at an excitation energy where the Zipf law is verified, it is interesting to perform such extensive study by comparing different centrality conditions and different size domains as in [21,22].

Besides these results, a large body of data has shown numerous signatures which are compatible with a coexistence phase of the liquid-gas type: negative branches of the heat capacity [24,25,26,27]; enhancement of equal-sized fragment partitions [28,29]; flattening of the caloric curve [30]; bimodality of the distribution of the largest or the asymmetry of the two largest fragments [31,32,33,34]. Moreover, recent experimental studies on central collisions of symmetric systems at bombarding energies around the Fermi energy have shown that data are compatible with a scenario in which a compression-expansion cycle leads to a spinodal decomposition of the system [29,35,36,37].

Thus, two types of interpretation could be given from the available nuclear multifragmentation data. The first one points to a critical phenomenon and the second one supports the picture of a system in the liquid-gas coexistence region of the phase diagram. This may not be contradictory since various processes might take place due to different explorations of the phase diagram and further studies are needed to investigate such a possibility. This situation has motivated the present analysis in terms of Fisher scaling, Zipf law and fragment observable fluctuations in measurements performed with the INDRA array. The data set used for the present analysis concerns fragmentation data from two kinds of centrality: quasi-projectiles produced in peripheral Au+Au reactions at 80 A MeV (denoted Au QP further on in the text) and mono-sources formed in central Xe+Sn collisions from 32 to 50 A MeV. In both cases, the sizes of the multifragmenting systems are comparable. Preliminary results using Fisher and Zipf techniques have already been reported elsewhere [38,39,40].

This paper is organized as follows: in Sec. 2, we describe succinctly the set-up of experiments and we present the methods used to select the events; Sec. 3 shows the results of the data analysis in the framework of the Fisher Droplet Model; in Sec. 4 the cluster size hierarchy is studied according to the Zipf law; in Sec. 5, fluctuations of cluster size and configurational energy are presented; in Sec. 6 we discuss the ensemble of the collected results. Conclusions are drawn in Sec. 7.

## 2 Experimental setup and event selection

### 2.1 Experimental setup

The $4\pi$ multidetector INDRA is described in detail in [41,42], and only the main specifications are listed here. INDRA is made of 336 detection cells arranged in 17 rings; the first one ($2^o$-$3^o$) is an array of phoswich scintillators. Rings 2 to 9 (polar angle from $3^o$ to $45^o$) consist of three layers comprising an ionization chamber (IoCh) followed by a solid state silicon detector (Si) and a cesium iodide scintillator (CsI(Tl)). The medium and backward angular ranges ($45^o$ to $176^o$) are covered with IoCh/CsI ensembles. The device provides a 90% of $4\pi$ geometrical efficiency, a charge identification from H to U, and a mass resolution up to beryllium. Data presented here have been obtained with INDRA installed at GANIL for Xe+Sn reactions between 32 and 50 A MeV and at GSI for Au+Au at 80 A MeV. For the experiment performed at GSI, a

$^{197}$Au beam was impinging a 2 mg/cm$^2$ $^{197}$Au thick target. The INDRA configuration used at GSI differs from the one used at GANIL only by the detectors of the first ring (2$^o$-3$^o$). At GSI, the phoswich scintillators were replaced with 12 Si-CsI(Tl) telescopes, each consisting of a 300 $\mu$m Si detector followed by a CsI(Tl) scintillator of 14 cm length. Further details of the experimental and calibration procedures can be found in [41,42,43,44].

## 2.2 Event selection

In Xe+Sn reactions, the set of collisions leading to multifragmenting monosources has been selected requiring that at least 80% of the total charge and momentum were measured. On this sample we have performed an event by event shape analysis based on the 3-dimensional kinetic energy flow tensor, calculated in the centre of mass frame of the reaction. The tensor is built with fragments with Z$\geq$5 and starting from M$_{frag}$$\geq$1. We have defined the $\theta_{flow}$ angle between the beam axis and the eigenvector associated with the largest eigenvalue of the diagonalized tensor. A flat cos$\theta_{flow}$ distribution is observed for $\theta_{flow}$$\geq$60$^o$ indicating a strong degree of equilibration. Thus this sample was retained for the analysis. More details are given in [45].



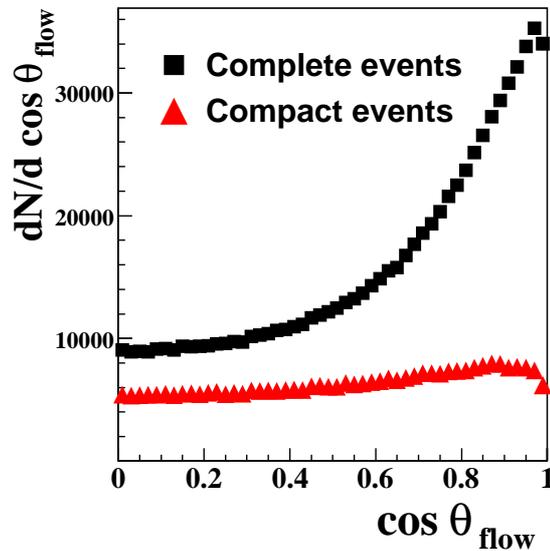Fig. 1. *$\theta_{flow}$ angle distributions for QP formed in Au+Au reactions at 80 A MeV in the QP reference frame. Full squares show the flow angle distribution for complete quasi-projectile events. Triangles represent the events selected according to the procedure explained in the text.*

Events comprising at least one fragment with Z $\geq$5 have been considered in the analysis of Au QP. We choose this value to be consistent with the
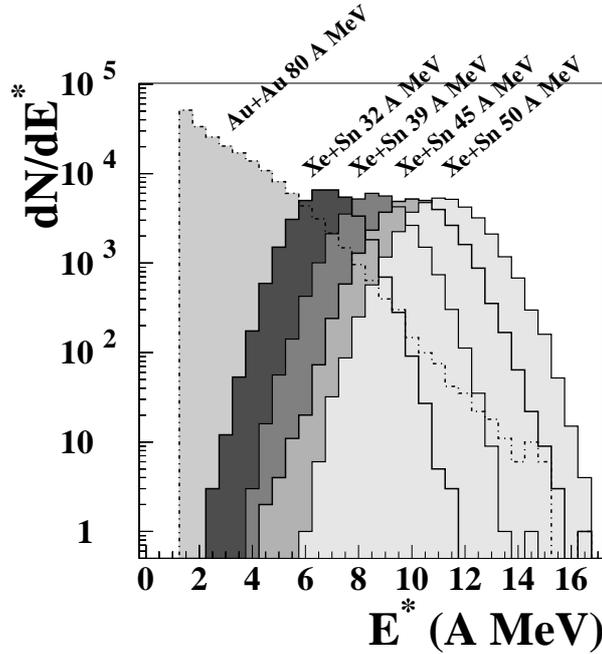
Fig. 2. *Excitation energy distributions for Au QP and Xe+Sn mono-source events between 32 and 50 A MeV.*

Xe+Sn mono-source analysis. The kinetic energy tensor is calculated event-by-event and gives the main axis of the event. A forward hemisphere with respect to this main axis can thus be defined. The total detected charge $Z_{tot}$ and the pseudo total momentum $P_{tot}$ collected in the forward hemisphere are calculated by summing up all the charged products having a positive velocity component along the main axis. Events satisfying $0.8 \times Z_{proj} \leq Z_{tot} \leq 1.1 \times Z_{proj}$ and $0.6 \times P_{beam} \leq P_{tot} \leq 1.1 \times P_{beam}$ are kept for the analysis and are called "complete events". This criterion allows to keep roughly 35% of the total number of measured events. Then in order to minimize the contribution of dynamical component at mid-rapidity [32] and to well define a quasi-projectile, a compactness criterion based on velocities is applied. This method requires that events comprise at least 2 fragments with $Z \geq 5$ and is based on two variables $\beta_{QP}$ and $\beta_{rel}$ defined as follows:

$$\beta_{QP} = |\sum \vec{p^{(i)}}.c| / \sum E^{(i)}$$

and

$$\beta_{rel} = \frac{2}{M_{frag}(M_{frag} - 1)} \sum_{i>j} |\vec{\beta^{(i)}} - \vec{\beta^{(j)}}|$$

$\beta^{(i)}$ and $\beta^{(j)}$ are defined in the centre of mass and $E^{(i)}$ represents the total energy of particle $(i)$.

At this bombarding energy, 80 A MeV, events are defined as compact if $\beta_{QP}/\beta_{rel} > 1.5$ [46,47], (24% of the measured events). Fission events, char-
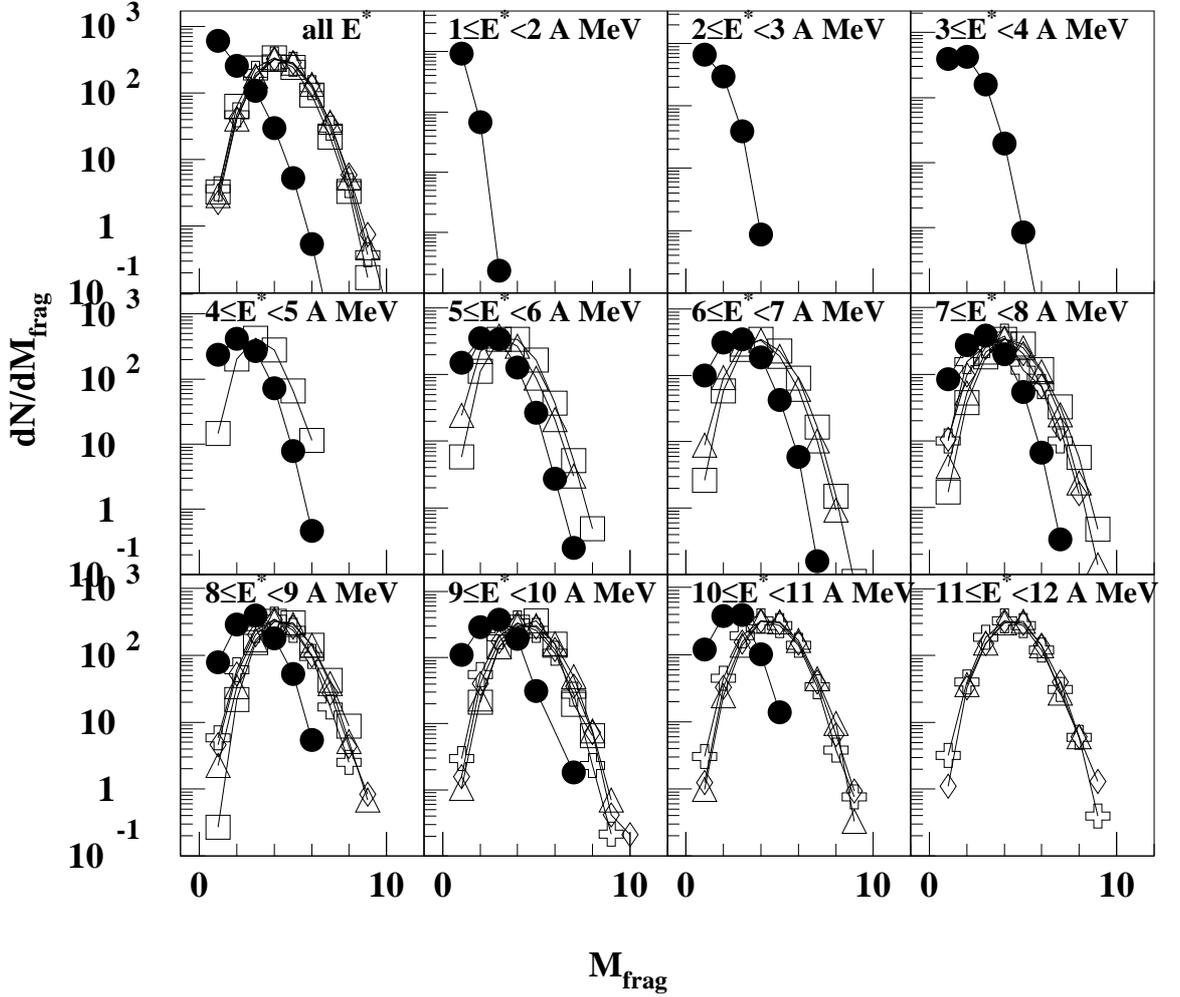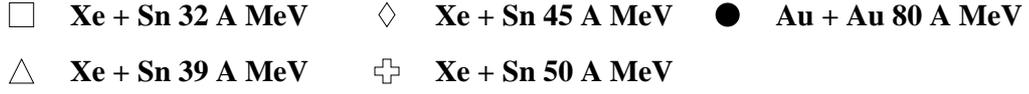
Fig. 3. *Top left panel, total fragment (Z≥5) multiplicity distributions for Au quasi-projectiles and Xe+Sn mono-sources. In the other panels, events are sampled into bins with 1 A MeV width in excitation energy.*

acterized by $Z_1 \times Z_2 \geq 900$, where $Z_1$ and $Z_2$ are the first and the second largest fragments, are rejected [48]. These events occur mainly at excitation energies lower than 3 A MeV. We have checked that the fission fragments have been properly excluded using a Campi plot as in [49]. Twice the charge of the light products emitted in the QP forward hemisphere is added to the sum of the fragment charges to obtain the charge of the quasi-projectile $Z_s$. Finally we keep events with $90\% \times Z_{tot} \leq Z_s \leq 100\% \times Z_{tot}$. The considered sample of events exhausts roughly 5% of the total measured events: in the whole procedure, the requirement of having a well characterized size is the most constraining. More

details are given in a forthcoming paper [46].

It is important to check what is the degree of equilibration reached in the ensemble of sources under investigation. This has been deeply studied and widely documented for Xe+Sn mono-sources [26,35,36,37,45,50], therefore only the procedure for Au quasi-projectiles is briefly presented here. The distribution of the flow angle $\theta_{flow}$, recalculated in the source frame, has been chosen to illustrate the degree of memory loss of the entrance channel in the selected collisions. Results of the analysis are presented in figure 1. Full squares represent the flow angle $\theta_{flow}$ distribution for complete quasi-projectile events as defined above. Here one clearly observes the typical behaviour of an ensemble of collisions dominated by dynamical effects and strongly focused on the beam direction. Triangles are for the $\theta_{flow}$ distribution of the selected ensemble. The $\theta_{flow}$ distribution is flat showing that there is no longer any privileged direction in the disintegration of the system and thus the set of data is compatible with the disintegration of an equilibrated source.

In the following, the analysis is performed as a function of the excitation energy $E^*$ using the calorimetric methods described in [26,47,51]. Accuracy on the calculated excitation energy is about 10% [51]. The excitation energy distributions are plotted in figures 2 for the events selected in the present analysis. For Xe+Sn mono-sources they exhibit a Gaussian shape with a mean value which increases with the incident energy. For Au QP, the $E^*$ distribution extends from 1 to 15 A MeV. The shape reflects the range of the impact parameter with the highest yield for the peripheral collisions. However due to the bombarding energy range (32 to 50 A MeV for Xe+Sn central collisions, both types of reaction cover a very similar range in excitation energy $E^*$. For each $E^*$ it is then possible to calculate some relevant observables such as, for example, the size of the source $Z_s$ or the fragment multiplicity $M_{frag}$. We point out that the mass of the source $A_s$ is derived from $Z_s$ assuming that its N/Z ratio is the same as that of the complete system. The average size of the source is around $<Z>\simeq80$-$85$ (with RMS$\simeq8$-$9$) for the Xe+Sn mono-sources and $<Z>\simeq72$ (with RMS$\simeq5$ due to the selection criterion 90%$\times Z_{tot} \leq Z_s \leq 100\% \times Z_{tot}$) for the selected Au QP.

Figure 3 shows the fragment multiplicity distributions for 1 A MeV $E^*$ bins. The top left panel represents the whole distribution integrated over excitation energy. The open symbols (full circles) are used for Xe+Sn mono-sources (Au QP). In Xe+Sn cases, $M_{frag}$ distributions are weakly shifted towards higher values when the excitation energy increases independently of the incident energy. For excitation energy $E^* \geq 4$ A MeV the fragment multiplicity distributions in Au+Au are peaked at a slightly smaller value in comparison

8

to Xe+Sn and the difference tends to increase as $E^*$ increases. The same trend persists even if $M_{frag}$ is normalized to the size of the source. On the top left panel the fragment multiplicity distributions are clearly different just because of the different ranges of excitation energy, (see figure 2).
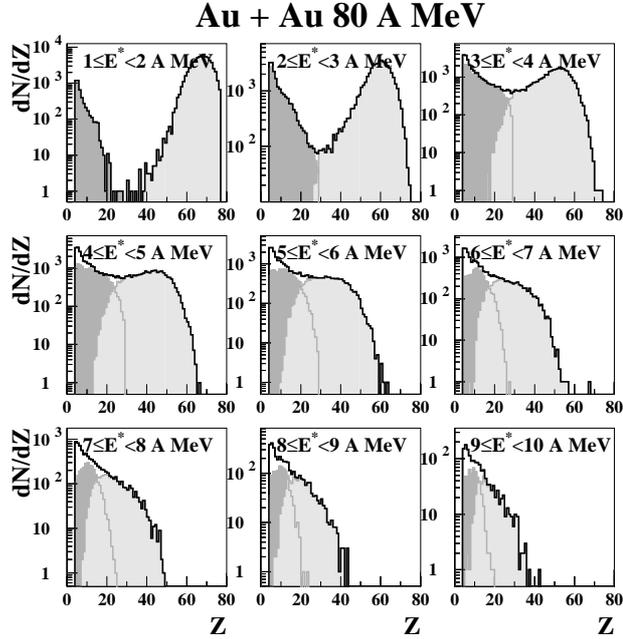


Fig. 4. *Charge distributions, starting from $Z \geq 5$, for QP formed in Au+Au reactions at 80 A MeV and selected according to the procedure explained in the text. Events are sampled into bins with 1 A MeV width in $E^*$ (the bin boundary is indicated). Light (dark) grey histograms represent the first (second) largest fragment extracted event-by-event. Black histograms are the complete charge distributions. Removal of fission events is explained in the text.*

Figures 4 and 5 present the excitation energy dependence of the charge distributions for quasi-projectiles produced in the Au+Au reactions at 80 A MeV and for Xe + Sn mono-sources at 32 A MeV, respectively. In both figures light (dark) grey histograms represent the first (second) largest fragment extracted event-by-event and black histograms are the total charge distributions. In the case of Au QP at low excitation energy one observes the typical U-shape of an evaporation process with a big residue and lighter fragments. As the excitation energy increases the intermediate charge range is gradually populated. At the highest excitation energy the charge distribution falls-off exponentially. The charge distribution in the case of Xe + Sn mono-sources presents a similar evolution in the common range of excitation energy. Size distributions of the two largest fragments extracted event-by-event are also shown. The qualitative behaviour is similar for central and peripheral collisions, but from figures 4 and 5 it appears that the shape of distributions of the largest fragments are different with a wider distribution in case of the QP data. This aspect will be
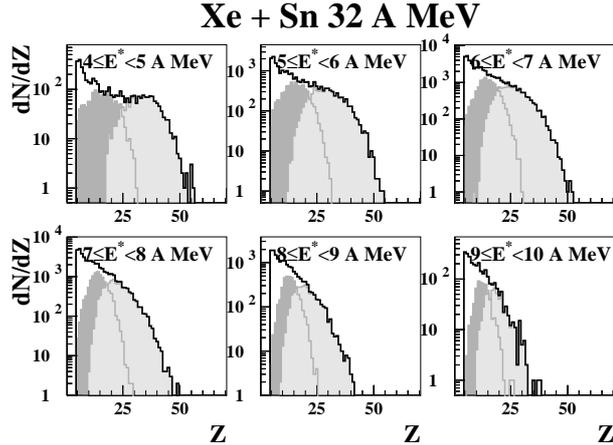
9

Fig. 5. *Charge distributions, starting from Z≥5, for Xe+Sn mono-sources at 32 A MeV. Events are sampled into bins with 1 A MeV width in excitation energy (the bin boundary is indicated). Light (dark) grey histograms represent the first (second) largest fragment extracted event-by-event. Black histograms are the complete charge distributions.*

discussed in more details in Section 5.

## 3 Data analysis with the Fisher Droplet Model

### 3.1 Parameterization using Fisher Droplet Model

The Fisher Droplet Model (FDM) [11,52,53] describes a gas of noninteracting clusters in thermal equilibrium with a liquid fraction. In this approach, the relative abundance of a cluster containing $A$ nucleons is given by:

$$\eta_A = q_0 A^{-\tau} exp(\frac{A\Delta\mu}{T} - \frac{c_0 \varepsilon A^\sigma}{T}) \qquad (1)$$

where $\eta_A = N_A/A_s$ is the average number of clusters of mass A per event, normalized to the system size $A_s$ and $q_0$ is the normalization factor; $\tau$ is the topological critical exponent and $\sigma$ is the critical exponent related to the ratio of the dimensionality of the surface to that of the volume; $\varepsilon = (T_c - T)/T_c$ measures the distance from the critical temperature; $\Delta\mu$ is the difference in chemical potential from the liquid phase and $c_0$ is the surface energy coefficient. Within the model, at the coexistence line $\Delta\mu = 0$ and at the critical point ($\varepsilon = 0$) a power law $q_0 A^{-\tau}$ is expected for the fragment mass distribution.

10

In the present work we take $T = \sqrt{8 \times E^*}$ assuming a Fermi gas (the total excitation energy is $E^* \times A_s$) as it is done in [18]. In the same reference it has been shown than the values of the critical parameters do not depend of the details of the caloric curve. $\Delta\mu$ and $c_0$ have been parameterized as polynomials of order 4 and 1 in $E^*$ respectively. The parameters $\tau$, $\sigma$, $c_0$, $\Delta\mu$, $E_{crit} = A_s \times T_c^2/8$ and the coefficients of the polynomial were allowed to vary in order to minimize the $\chi^2$. This formulation differs slightly from the one used by the authors of [13,14,18]. However, it was checked that $E_{crit}$, $\tau$ and $\sigma$ parameters are not very sensitive to the details of the scaling function as shown in [18]. Indeed this feature makes the Fisher scaling analysis a very appealing technique to compare data samples and extract universal behaviours.
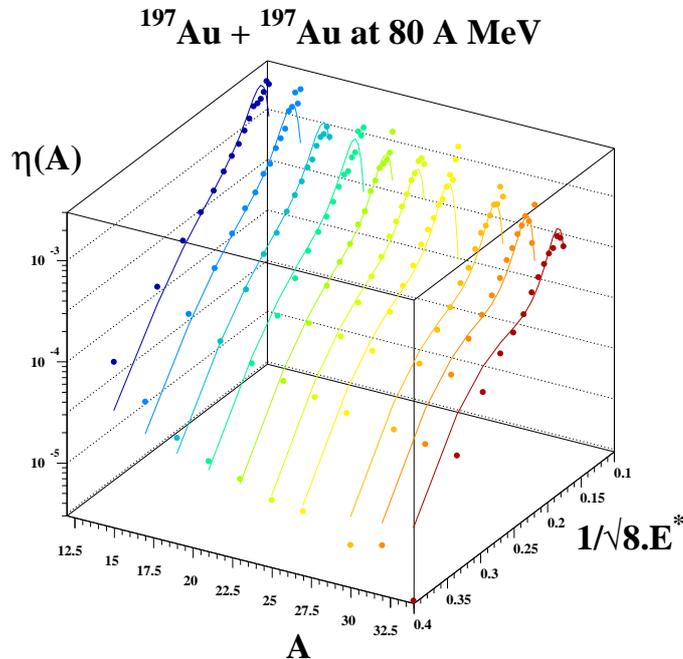
### 3.2 Experimental results



Fig. 6. *Yield surface $\eta_A$ as a function of A and $1/\sqrt{8.E^*}$. Lines are the results of the fitting procedure to the Fisher model for charge ranging from Z=6 to 15.*

The results of the fit are shown in figure 6 where data (circles) and fits (curves) are reported in a three dimensional plot ($\eta_A$, $A$, $1/\sqrt{8.E^*}$). The quality of the fit is rather good over a large range of size $A$ and excitation energies $E^*$ and the main features of the excitation functions are reproduced. The next step consists in using the scaling properties contained in the Fisher Droplet Model parameterization to reduce all the information. This is shown in figure 7 where $\eta_A/(q_0 A^{-\tau}) \times exp(A\Delta\mu/\sqrt{8.E^*})$ is plotted against $\varepsilon A^\sigma/\sqrt{8.E^*}$. Now the experimental data from Au QP collapse in a single line. The Fisher Droplet parameterization is applied to the fragmentation of mono-sources produced in

Table 1

*Values of the critical exponents $\tau$, $\sigma$ and of $E_{crit}$ extracted from the Fisher Model Analysis for the experimental data studied. The value of $\Delta\mu$ and $E_{crit}$ are indicated in parentheses when they point out of the range covered by the data set.*

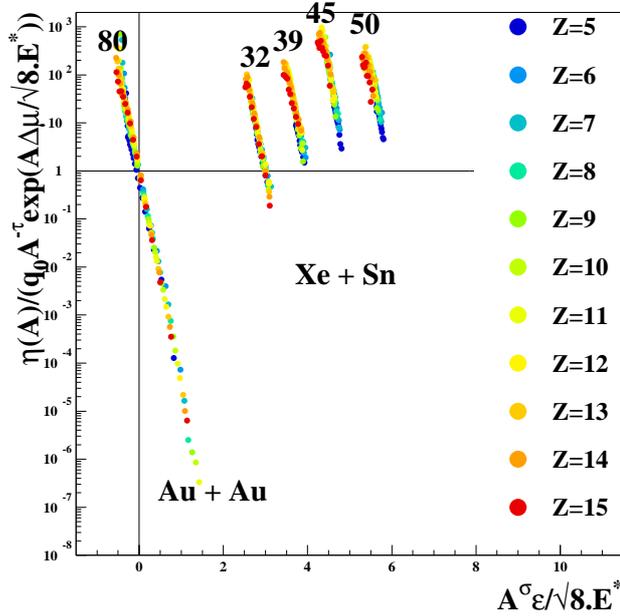| System | $\tau$ | $\sigma$ | $E_{crit}(AMeV)$ | $\Delta\mu$ at $E_{crit}$ | $\chi^2$ |
|---|---|---|---|---|---|
| **Xe + Sn 32 A MeV** | 2.09±0.01 | 0.66±0.01 | 4.50±0.03 | 0.33 | 2.1 |
| **Xe + Sn 39 A MeV** | 2.38±0.02 | 0.66±0.01 | 4.49±0.03 | 0.19 | 2.8 |
| **Xe + Sn 45 A MeV** | 2.40±0.03 | 0.66±0.01 | (3.79±0.03) | (0.90) | 2.7 |
| **Xe + Sn 50 A MeV** | 2.35±0.02 | 0.65±0.01 | (4.23±0.04) | (-0.02) | 5.7 |
| **Au + Au 80 A MeV** | 2.56±0.02 | 0.66±0.01 | 4.20±0.03 | 0.24 | 9.7 |



Fig. 7. *Scaled yield distributions for Au QP events, Xe+Sn mono-sources. Bombarding energies in A MeV are reported on top of each scaled distribution. A horizontal shift is added for each Xe+Sn system (+3, +4, +5, +6 respectively) to visualize the scaled distributions.*

central Xe+Sn collisions. For each bombarding energy the scaled yields fall on the same line (they have been shifted in figure 7 for better visualization) meaning that they can be described with the exponential dependence of the Fisher Droplet Model. This scaling feature was also observed in other recent works [13,14,18,38,40,54]. The values obtained from the fit, $\tau$, $\sigma$ and $E_{crit}$ are reported in Table 1 together with those of $\chi^2$. The value of $\Delta\mu$ and $E_{crit}$ are indicated in parentheses when they are out of the range covered by the data set. Both $\tau$ and $\sigma$ values are in the range predicted by the Fisher Model and are consistent with other experimental works. The parameter $E_{crit}$ is around

4-4.5 A MeV for all systems analysed here. This value is commonly obtained in all analyses based on the Fisher scaling technique. In the present data $E_{crit}$ are quite similar whatever the centrality of the collision and no noticeable role of the entrance channel dynamics on the extracted parameters is observed. This result agrees with [18] in which peripheral and central collisions were investigated through the Fisher scaling technique.

Looking at the results in more details one sees that $\Delta\mu$ is slightly positive at $E_{crit}$ (see Tab.1), which means that the size distribution at $E^*=E_{crit}$ does not follow exactly a power law $\eta_A = q_0 A^{-\tau}$. If a two parameters ($q_0$ and $\tau$) power law fit is performed on the charge distributions at the critical energy, one obtains a $\tau$ value which is much lower ($1<\tau<1.5$) than the one extracted using the scaling analysis [38]. This difficulty prevents any determination of the phase diagram, the location of the coexistence region, and the extraction of the critical point, conversely to what has been done in [13,14]. We will come back on the interpretation of the Fisher scaling in the general discussion of section 6.

## 4    Cluster size hierarchy and Zipf law

Originally the Zipf law was used to analyze the relative population of words in texts. The frequency of the word is inversely proportional to its rank in a frequency list [19]. The integer rank n is defined starting from 1 for the most probable. Later, many applications of this relationship were made in a broad variety of areas, such as city-population distributions, sand-pile avalanches, the distribution in strengths of earthquakes, the genetic sequence, etc. It has been suggested that the existence of similar linear hierarchy distributions in these very different fields indicates that the Zipf law is a fingerprint of criticality. In particular, recent investigations with Lattice Gas Model [5] have shown that the cluster distribution follows a Zipf law at the critical point. In this case the analysis was shifted from the frequency to the cluster size. This has raised a strong interest around this observable and a Zipf law has been observed in the multifragmentation of a quasi-projecile of Ar in conjunction with other signatures of critical behaviour, leading the authors to conclude that the nuclear system has been observed at or close to the critical point [22].

In the present study we explore the applicability of the Zipf law to heavy excited systems of similar size formed either in central or peripheral collisions. For each $E^*$ bin of 1 A MeV width, the value of $<Z_n>$ is calculated for each rank n. We first consider the fragments with Z≥3. The energy dependence of all $<Z_n>$ is fitted using the formula $<Z_n> \simeq n^{-\lambda}$ for n≤6 to have a good

statistic. This procedure provides the evolution of $\lambda$ with $E^*$ and allows to localize the excitation energy $E_{Zipf}$ where the exact Zipf law is satisfied ($\lambda$=1).

**Xe + Sn 39 A MeV**
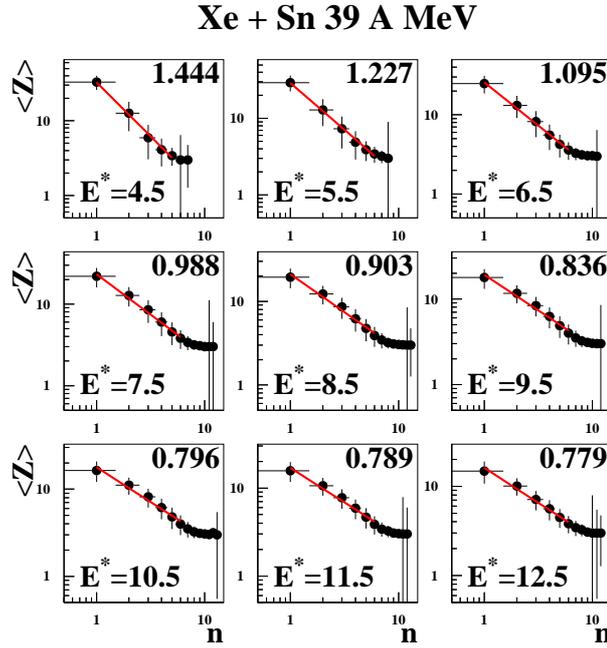


Fig. 8. *For Xe+Sn at 39 A MeV, $<Z>$ versus rank n, in decreasing charge order, for different bins of $E^*$ (the mean value of the bin is indicated). The fit $<Z_n> \simeq n^{-\lambda}$ is represented by the line and the $\lambda$ value is indicated in the right upper part of each panel.*

Results are shown on figure 8 for Xe+Sn mono-sources at 39 A MeV. Similar results are obtained at other incident beam energies discussed in this article. The $\lambda$ values extracted from the fit are reported in the right upper part of each panel. Figure 9 shows the $\lambda$ dependence as a function of $E^*$. The main feature extracted from figure 9 is a monotonic decrease of the $\lambda$ parameter with increasing $E^*$. At 32 and 39 A MeV, the Zipf law is satisfied at $E_{Zipf}$=$E^*\simeq$7.5 A MeV. As the excitation energy increases $\lambda$ stays below unity. The same procedure is applied to Au QP. The obtained values do not superimpose on the ones extracted from Xe+Sn mono-sources and $\lambda$=1 is reached at a higher energy $E_{Zipf}\simeq$8.5 A MeV.

We have also considered the influence of the minimal value of the charge used for the analysis. This is all the more important that the charge asymmetry is different in both systems, see next section. With increasing minimal charge both curves of figure 9 shift towards lower excitation energy. The shift is even larger for Au QP. Indeed for Z≥4 both curves superimpose and we obtain $E_{Zipf}$=$E^*\simeq$6.5 A MeV.

According to [5] and based on the prediction of the Lattice Gas Model, the Zipf energy, $E_{Zipf}$, would be one of the characteristics of the critical point. In our data the "critical energies" found, $E_{Zipf}$ and $E_{crit}$, using the Zipf-like and Fisher-like analysis are not consistent.
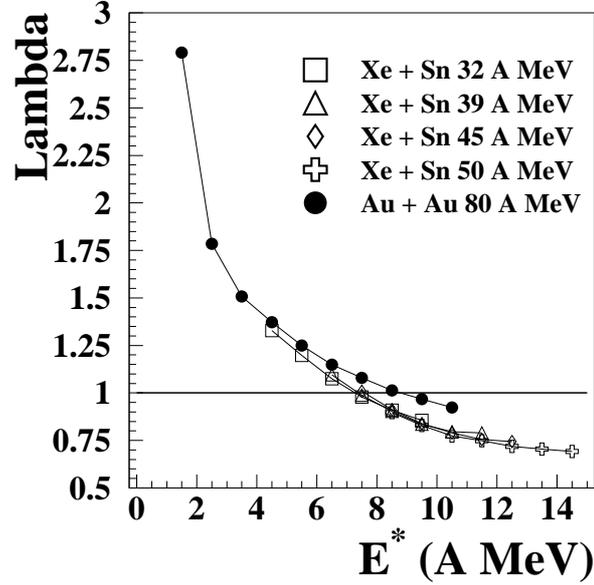


Fig. 9. $E^*$ dependence of the $\lambda$ parameter extracted from the fit $<Z_n> \simeq n^{-\lambda}$ for Xe+Sn at 32, 39, 45 and 50 A MeV mono-sources and Au QP events at 80 A MeV. The Zipf law is satisfied when $\lambda=1$ (horizontal line).

## 5 Cluster size and kinetic energy fluctuations

### 5.1 Largest and second largest fragment.

Maximal fluctuations in fragmentation data are actively searched for since it is believed that they would be observed in the coexistence region or close to the critical point [55]. In this part we will show new results on properties of the largest fragment, since various experimental and theoretical works suggest that the largest fragment can be associated with an order parameter for the phase transition [56].

Figures 10 and 11 show the evolution of the average charge of the largest, $<Z_1>$ and second largest, $<Z_2>$, fragment as a function of the excitation energy $E^*$ for Au QP and Xe + Sn mono-sources at 32, 39, 45 and 50 A MeV.
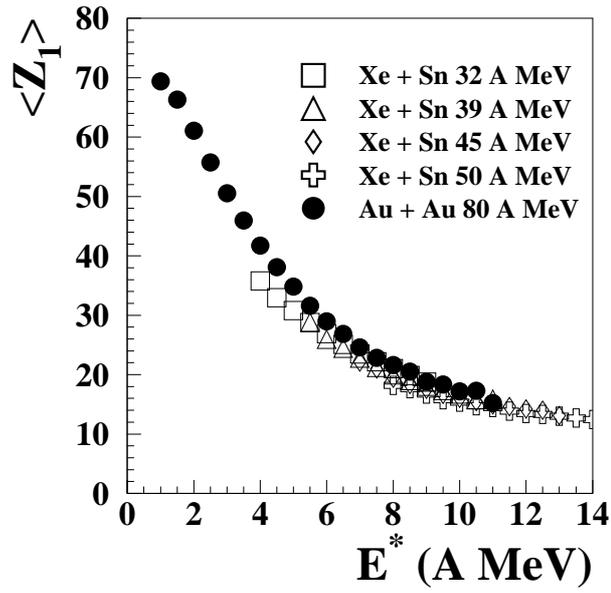
Fig. 10. *Evolution of the average charge of the largest fragment as a function of the excitation energy E\* for Xe+Sn at 32, 39, 45 and 50 A MeV mono-sources and Au QP events.*
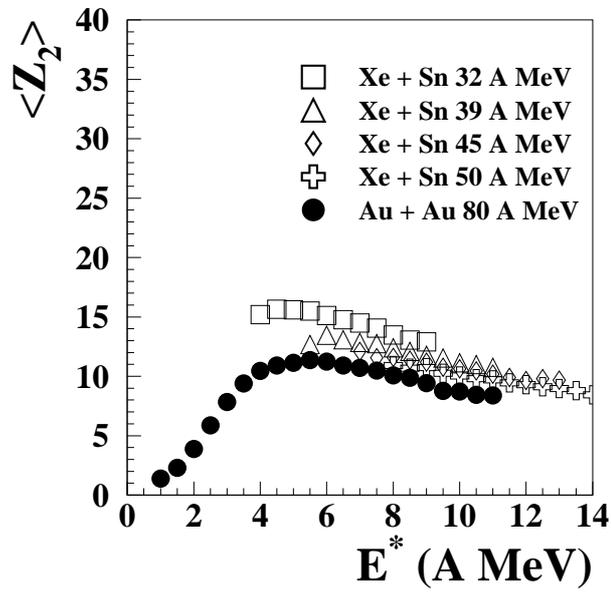


Fig. 11. *Evolution of the average charge of the second largest fragment as a function of the excitation energy E\* for Xe+Sn at 32, 39, 45 and 50 A MeV mono-sources and Au QP events.*

16

The source size for Au QP events is $<Z_s>=72$ and for Xe+Sn mono-sources it has values of $<Z_s>=83, 81, 79, 79$ for 32, 39, 45 and 50 A MeV bombarding energy, respectively. For Au QP, $<Z_1>$ decreases from a value very close to the projectile charge for $E^*\simeq1$ A MeV down to $<Z_1>=15$ at $E^*=12$ A MeV. Data from Xe+Sn mono-sources are presented as open symbols in figure 10. Although the Au source is smaller, one observes that the corresponding $Z_1$ values are slightly larger than the Xe+Sn ones. At $E^*=4$ A MeV the difference is around 6 charge units and becomes negligible around 10 A MeV. Thus there is no scaling of the charge of the largest fragment with the source size.

Figure 11 shows the evolution of the average charge of the second largest fragment (including light charged particles), $<Z_2>$, as a function of excitation energy $E^*$ for Au QP (filled circles) and Xe + Sn mono-sources at 32, 39, 45 and 50 A MeV (open symbols). For the QP data, one observes a rise and fall with a maximum at $E^*\simeq5$ A MeV. This feature is not surprising; it is known that at very low excitation energy, in the evaporation regime, $<Z_2>$ is close to one-two. Increasing with the opening of the fragment-evaporation channel, $<Z_2>$ reaches a maximum when multifragmentation becomes dominant. It then slowly decreases similarly to $Z_1$ at large $E^*$. Thus a maximum is expected for this observable on a range of $E^*$ as it is the case for Au QP. Comparing both data sets at the same $E^*$, one observes higher $<Z_2>$ values for mono-sources, particularly at 32 A MeV. For higher bombarding energy up to 50 A MeV, all values of $<Z_2>$ roughly collapse on a single curve and decrease linearly as $E^*$ increases. Finally, at a given excitation energy the asymmetry between the two largest fragments is higher for the Au QP.

Besides this global analysis it is interesting to look at which energy $<Z_2>$ is exactly equal to $<Z_1>/2$. Indeed it has been shown in [22] that for the Ar quasi-projectile, the relationship between $<Z_1>$ and $<Z_2>$ has a bell shape. The maximum is at $<Z_2> = <Z_1>/2$ and is observed at an excitation energy $E^*$ for which the Zipf law is verified. Figure 12 shows the relationship between the two largest fragments measured in peripheral Au QP (filled circles) and in Xe+Sn mono-sources (open symbols). The line represents the locus where $<Z_2>=<Z_1>/2$. A bell shape is observed for Au QP events. At the maximum $<Z_1>\simeq30$ and $<Z_2>\simeq12$: These values refer to an excited source at $E^*=6$ A MeV (see figure 10 and figure 11) significantly below $E_{Zipf}=8.5$ A MeV. However above $E^*=8$ A MeV, the relation $<Z_2> = <Z_1>/2$ is verified. Thus our data on Au quasi-projectiles do not lead to the coherent picture seen in the fragmentation of an Ar quasi-projectile [22]. For Xe+Sn mono-sources at 32 A MeV, $<Z_2>=<Z_1>/2$ is verified only at the maximum but it corresponds to $E^*= 5$ A MeV, a value far below $E_{Zipf}=7.5$ A MeV for mono-sources. In the other Xe+Sn mono-sources, we do not find data supporting the coherence seen in [22]. At this stage of the analysis, one could suggest
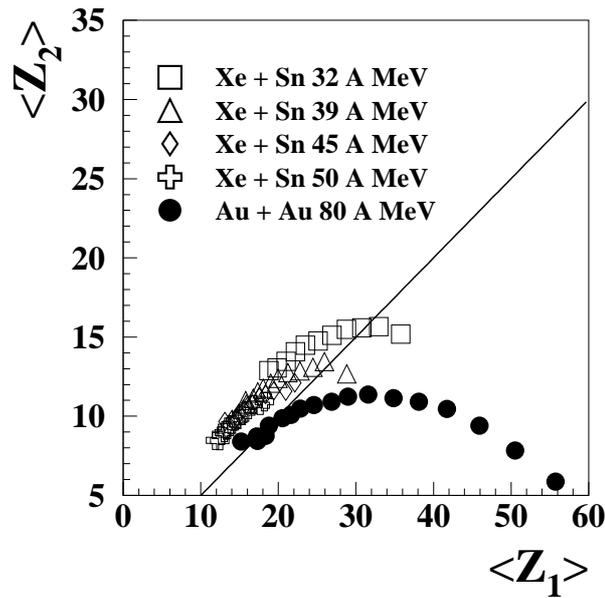
17

Fig. 12. *Average size of the second largest fragment $<Z_2>$ as a function of the average size of the largest fragment $<Z_1>$ for Xe+Sn at 32, 39, 45 and 50 A MeV mono-sources and for quasi-projectiles measured in Au+Au reactions at 80 A MeV. The line corresponds to $<Z_2> = <Z_1>/2$.*

a possible influence of the size of the sources between Ar quasi-projectiles and the present systems which are more than four times larger.

## 5.2 Fragment size fluctuations

It is expected that close to the critical point fluctuations in the cluster size distribution are maximum. It is suggested in various models that the fluctuations in the size of the largest fragment could be a good indicator of the distance of the system from the critical point, even for finite systems. In the experimental study of ref. [22] at the excitation energy where Zipf law is verified the authors observe also the largest value of the normalized fluctuations . In figure 13 are reported these fluctuations, $\sigma_{Z_1/Z_s} = \sqrt{<(Z_1/Z_s)^2> - <(Z_1/Z_s)>^2}$, as a funtion of $E^*$ as deduced from the present data set. For Xe+Sn mono-sources $\sigma_{Z_1/Z_s}$ continuously decrease. For Au QP $\sigma_{Z_1/Z_s}$ reaches a maximum value around $\simeq 4.5$ A MeV. The highest value of $\sigma_{Z_1/Z_s}$, $\simeq 0.135$, is in good agreement with other data [14] (see also table 3 in "Fluctuations of fragment observables" in [2]). Indeed in quasi-projectiles measured at 35 A MeV in Au+Au collisions with Multics, a $\sigma_{Z_1/Z_s}$ value of 0.14 is obtained and $\sigma_{Z_1/Z_s} \simeq 0.12$-0.13 for EOS data. The maximum is observed at an excitation energy very close to $E_{crit}$ extracted from the Fisher procedure and well below $E_{Zipf} \simeq 8.5$ A MeV
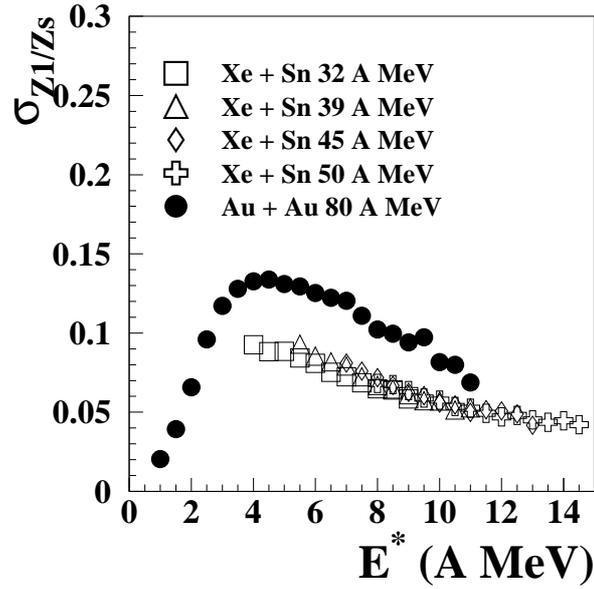
Fig. 13. *Fluctuations of the average size of the largest fragment normalized to the source size $Z_1/Z_s$ of the multifragmenting system as a function of the excitation energy for Xe+Sn mono-sources and Au QP events.*

extracted from the Zipf law fit. A striking feature is the superposition of all Xe+Sn data whatever the bombarding energy which confirm that the fragmentation pattern in Xe+Sn central collisions depends only on the excitation energy. Finally, the normalized fluctuations are systematically smaller for Xe+Sn mono-sources than for Au QP. It is very interesting to remark that, for a given value of deposited excitation energy, the Au QP data systematically show a lower degree of fragmentation. This is measured by the lower fragment multiplicity, figure 3, the higher charge asymmetry between the two heaviest fragments, figures 10 and 11 and the higher fluctuation, figure 13, associated to the Au QP data. This experimental finding points towards a different fragmentation scenario between the two data sets characterized by different entrance channels. Different physical reasons may be invoked: a different thermodynamic path in the temperature-pressure plane, an influence of the radial flow dynamics on the fragmentation pattern... Further studies will be needed to disentangle between the different interpretations and to investigate the influence of the asymmetry in the entrance channel and to explore a different size region.
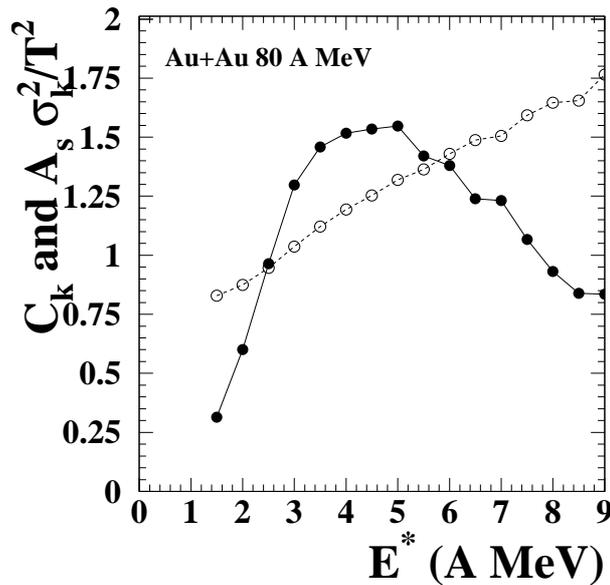
Fig. 14. *Normalized fluctuations $A_s\sigma_k^2/T^2$ (filled circles) and kinetic energy capacity $c_k$ (open circles) as a function of excitation energy for Au QP reactions at 80 A MeV.*

## 5.3 Configurational energy and heat capacity

For a finite system in the liquid-gas coexistence zone one expects large fluctuations of the total kinetic energy (supposed only thermally coupled to the system) leading to a negative value of the heat capacity [9,10,55,57]. For equilibrated excited nuclear systems one assumes that the total excitation energy $E^*$ can be separated in two components, $E^* = E_k + E_{pot}$, where $E_k$ and $E_{pot}$ are the total kinetic energy and total configurational energy respectively. The total heat capacity is defined as $c_{tot} = c_k^2/(c_k - A_s\sigma_k^2/T^2)$ where $c_k = dE_k/dT$; the temperature T is estimated by solving the kinetic equation of state [26,58] and $A_s$ is the size of the source. In multifragmentation studies the total kinetic energy $E_k$ should be determined at the freeze-out stage but such configuration is not experimentally accessible. However, one may deduce the heat capacity from the configurational energy of measured partitions, if side feeding effects are properly accounted for. The general procedure has been thoroughly checked and well developed in [27].

Results of the analysis are presented in figure 14 for Au QP. Normalized fluctuations $A_s\sigma_k^2/T^2$ (filled circles in figure 14) show a bell shape as a function of the excitation energy $E^*$ with a maximum around $\simeq 4$ A MeV. It is worth noticing that for Au QP events, fluctuation of the average size of the largest
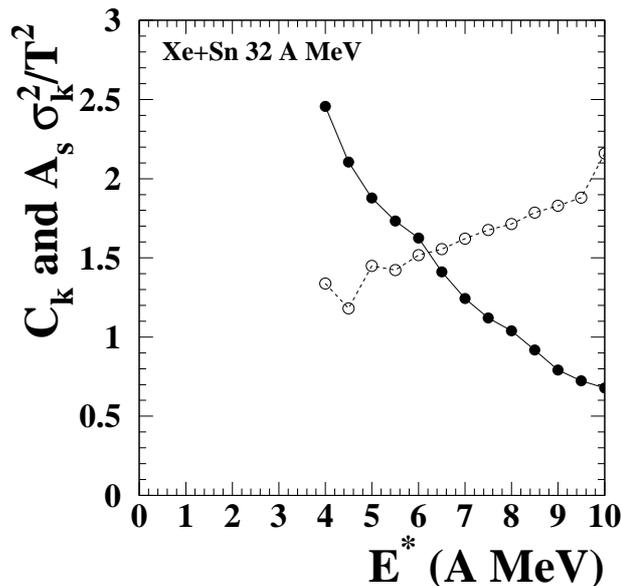
Fig. 15. *Normalized fluctuations $A_s\sigma_k^2/T^2$ (filled circles) and kinetic energy capacity $c_k$ (open circles) as a function of excitation energy for Xe+Sn mono-source events at 32 A MeV.*

fragment, normalized to the source size $Z_1/Z_s$, is maximum at roughly the same energy. $c_k$ (open circles in figure 14) monotonically increases with the excitation energy and crosses the normalized fluctuations at $E^*\simeq2.5$ A MeV and $E^*\simeq5.5$ A MeV. In the hypothesis of thermal equilibrium such crossings are associated with two divergences and a negative branch in the total heat capacity [9]. It has been shown in the literature, ([2] p.259 figure 8) and [32], that the magnitude of the fluctuations decreases when dynamical effects are present. As we have shown in figure 1, the sample selected with a compacity criterion exhibits a flat $\cos\theta_{flow}$ distribution which indicates that a strong degree of equilibrium is reached. Results shown in figure 14 are compatible with those found in Au QP for the same data at another selection of compact events [32] and by the MULTICS collaboration [24,27,58] but at 35 A MeV. Moreover, locations of divergences and maximal normalized fluctuations are observed at the same excitation energies in both INDRA and MULTICS data. Figure 15 shows the result of the analysis for Xe+Sn mono-sources at 32 A MeV. Due to the limited range of $E^*$, only the divergence at high excitation energy is observed but it is worth noticing that it is roughly at the same $E^*$ as in the Au QP events. As the incident energy increases the position of the second divergence remains constant but the negative part of the total heat capacity progressively disappears as we are exploring higher excitation energies.

# 6 Discussion

## 6.1 Summary of experimental findings on scaling, ordering and fluctuations of fragment observables.

Let us first recall our findings regarding pseudo-critical behaviours and fluctuations of fragment observables in Xe+Sn mono-sources and Au QP events. Applying the Fisher procedure a good scaling of the cluster yields is observed, providing the pseudo-critical energy $E_{crit}$ where a power law is observed, the value of the critical exponents $\tau$, in the range 2.09-2.56 and $\sigma \simeq 2/3$. For a liquid-gas transition $\tau$=2.21 for Ising 3D [59], for a mean field Lattice Gas $\tau$=2+1/D (=2.33 for a 3 dimensional Lattice). In an infinite 3D percolation $\tau$=2.18 [60] and $\tau$=2.2±0.1 in a finite one [61]. The value of $\tau$ does not provide a discriminating test for characterizing the universality class of the transition. In the present work the values of the critical energy are in the range 3.8-4.5 A MeV. Conversely, a Zipf law is observed for all systems but at an energy higher than $E_{crit}$: $E_{Zipf} \sim 7.5$ A MeV for Xe+Sn mono-sources and $E_{Zipf} \sim 8.5$ A MeV for Au QP events. The normalized fluctuations of the largest fragment exhibit a maximum around 4.5 A MeV. Finally, for the Au QP, the normalized kinetic fluctuations $A_s \sigma_k^2 / T^2$ reach a maximum around 4 A MeV. Within the framework of thermodynamic equilibrium, the heat capacity is negative between $E^*$=2.5 and $E^*$=5.5 A MeV. The present results agree with many works reporting numerous signatures compatible with a system in a mixed phase of liquid and vapor ([24,25,26,27,28,29,30,31,32,33,34,35,36,37,50]).

Several conclusions can be drawn out from our findings. First, for Au QP and Xe+Sn mono-sources, the "critical energies" extracted from Fisher and Zipf procedures are not compatible with each other. Such a conclusion is at variance with ref.[22]. Moreover, in our data, the Zipf law is observed at an excitation energy well above that where the fluctuations connected to the heat capacity are maximum. It was recently stated [23] that the Zipf law could be deduced from the power law behaviour of the cluster size distribution and the exponents $\tau$ and $\lambda$ would roughly satisfy $\lambda$=1/($\tau$-1) at the critical point, leading to $\tau$=2, a value below our experimental values and from most of the theoretical calculations (for example 3D percolation or Lattice Gas Model). In our data, $\tau$=2.2 gives $\lambda$=0.86, a value obtained at $E^*$=9.5 A MeV, higher than the excitation energy where Zipf law is verified and consequently even further from the critical energy obtained from the Fisher fitting procedure.

A more interesting remark is that the critical energy extracted from the Fisher procedure is located in the domain where the normalized fluctuations of the

largest fragment and the configurational energy fluctuations reach their highest values. This was clearly deduced from the Au QP, and could be only extrapolated from Xe+Sn mono-sources data since in such cases low excitation energies are not explored.

The Zipf law is not a reliable way to identify a system close to or at the critical point. Further investigations are needed to explain differences between our results and those shown in [22]. Size effects might be a possible direction to explore. Another interesting proposition from Bauer and collaborators is to replace the Zipf law by the Zipf-Mandelbrot law [62].

The results of Fisher scaling and negative heat capacity do not show any dependence on the type of collisions studied. Conversely, some differences appear in the energies where the Zipf law is verified and in the fluctuations of the largest fragment. This observation points to the specific role of the largest fragment as already observed in [37,50], which appears more sensitive to the fragmentation mechanism. Indeed these results suggest that for Au QP and Xe+Sn mono-sources the fragmentation mechanisms are different.

To go further in the discussion we used predictions of theoretical models as guidelines to understand our results.

*6.2 Guidelines from the Lattice Gas Model*

This model is well known to describe a first as well as a second order phase transition. Since thermodynamical conditions of the model are well defined (temperature, energy, density, coexistence line, critical point) it is straightforward to verify whether a Fisher scaling is observed in the Lattice Gas Model, and how to interpret the "Fisher critical point" in such a framework. A Fisher procedure [8] was performed at different densities (critical, subcritical and supercritical). A very good scaling is observed for all densities but the critical temperature extracted from the fit is density dependent. The analysis of ref. [8] is analogous to the one we have carried out with the data. In this case, it would be better to describe the derived power law as a pseudo critical behaviour since it is not only observed at the critical point but also inside as well as outside the coexistence region. Gathering the results in a temperature-density plot, one finds that the locus of the pseudo-critical points is close to the so called Kertesz's line [63,64]. Thus the observation of a Fisher scaling is not a tool to determine the location of the critical point. However, the Fisher scaling is compatible with fragmentation inside the coexistence region,

in agreement with our experimental indications from configurational energy fluctuations. Moreover the narrow range of $E^*_{crit}$ in our analysis suggests, in the framework of the Lattice Gas Model, that a narrow range of density is explored by the studied systems.

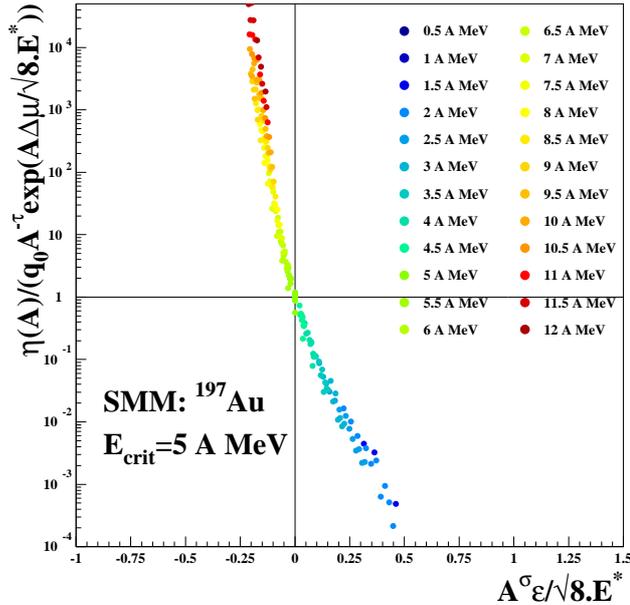### 6.3  Guidelines from the Statistical Multifragmentation Model SMM



Fig. 16. *Fisher scaling for SMM events.*

We have performed a Fisher procedure on the predictions of a well known statistical multifragmentation model (SMM). A detailed description of SMM can be found in [65]. The basic assumption of the model is the statistical distribution of the breakup channels of a decaying system at thermal equilibrium. SMM was largely used to reproduce the characteristics of multifragmentation events [25,48]. In the present work, calculations have been performed, for a fixed value of the source ($Z_0$=79, $A_0$=197) at two freeze-out volumes ($V_{fo}$= $3V_0$ and $6V_0$) and for a flat distribution of excitation energy in the range $0.5 \leq E^* \leq 12$ A MeV. The experimental filter has not been applied to the predictions of the model since our goal was not to reproduce the data.

We first applied the Fisher procedure to the calculations. The yield parameterization is the same as the one used to study the experimental data (see section 3). Predictions at $V_{fo}$= $3V_0$ are shown in figure 16 where $\eta_A/(q_0 A^{-\tau}) \times exp(A\Delta\mu/\sqrt{8.E^*})$ is plotted against $\varepsilon A^\sigma/\sqrt{8.E^*}$. Here for the caloric curve we assume the same ansatz as for the experimental data. In the framework
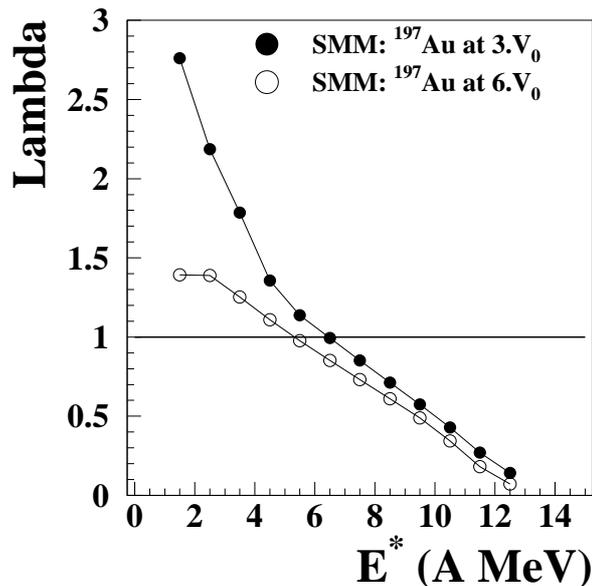
Fig. 17. *Zipf analysis for SMM calculations.*

of SMM we have access to an average temperature corresponding to a given excitation energy. We have observed that in our calculations the caloric curve (similar to the one shown in figure 1 in [66]) is close to the one obtained in [18]. It was demonstrated in [18] that the values of the extracted critical parameters do not depend on the shape of the caloric curves. Results of the calculations fall on a single curve, which is not a straight line at variance with the experimental data (indeed in SMM the $c_0$ coefficient deduced from the fit procedure evolves rapidly with $E^*$, whereas it appears roughly constant in the data) and thus a scaling law is observed for SMM events. Fisher "critical point" is obtained at $E^* \simeq 5$ A MeV. This model presents a phase transition of first order [57], meaning that in this case the power law behaviour as well as the scaling cannot be connected to the location of a critical point. They rather signal a maximal fluctuation point. Indeed under the microcanonical constraint kinetic energy fluctuations are maximum when the configuration energy has the largest spread, i.e. when the size distribution is close to a power law. Therefore, in the statistical multifragmentation model, the Fisher "critical point" can be interpreted as the energy where fluctuations are maximum. This is in agreement with our experimental findings. Finally, the analysis performed at $V_{fo}=6V_0$ does not indicate a noticeable freeze-out volume influence on the scaling properties nor on the parameters extracted from the Fisher fit ($E_{crit}$, $\tau$ and $\sigma$).

The Zipf law fit has also been performed on SMM events using the same protocol as for experimental data. Results of the analysis are presented in figure 17 for $V_{fo}= 3V_0$ (filled circles) and $6V_0$ (open circles). For both freeze-out
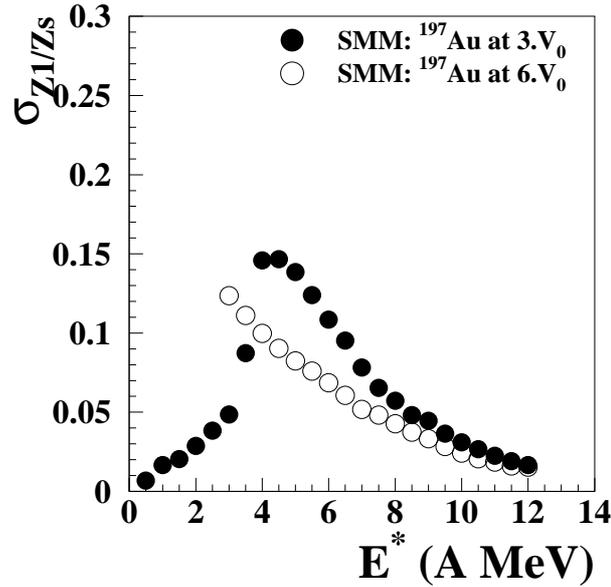
Fig. 18. *Fluctuations of the average size of the largest fragment normalized to the source size $Z_1/Z_s$ as a function of the excitation energy for SMM calculations.*

volumes we observe a decrease of the $\lambda$ parameter as the excitation energy $E^*$ increases. When $V_{fo} = 3V_0$, $\lambda=1$ is reached at $E^*=6.5$ A MeV, a value which falls in the region close to the second divergence of the heat capacity. At variance with the Fisher fitting procedure, the Zipf law fit seems to evolve with the freeze-out volume. As indicated in figure 17, one observes a shift towards lower excitation energy as $V_{fo}$ increases. The value found in this case, $E_{Zipf}=5$ A MeV, is comparable with the one extracted from the Fisher procedure, $E_{crit} \simeq 4.5$ A MeV. All the trends and values shown in figure 17 are similar when the analysis is performed for fragments at the freeze-out stage. We can mention that the same volume effect was seen in [5] for the occurrence of the Zipf law as a function of the density in the Lattice Gas Model. Values of $E_{Zipf}$ obtained from SMM fall below the experimental ones for both sets of data. Figure 17 however suggests that the present Au QP data may be associated with smaller freeze-out volumes. To investigate the potential role of the freeze-out volume on the Zipf procedure, one needs other theoretical tools.

Figure 18 represents the normalized fluctuations of the charge of the largest fragment $\sigma_{Z_1/Z_s}$ as a funtion of $E^*$ deduced from SMM calculations for the two volumes. Because of the presence of fission, the points for $V_{fo}=6V_0$ are not displayed below 3 A MeV in figure 18. The observed trend is very similar to the one seen in figure 13 which again indicates a smaller volume for Au QP. It has been shown indeed that the volume influences the size of the biggest fragment [67]. More specifically, the normalized fluctuations reach a maximum

value at E*=4.5 A MeV for a source at $V_{fo}=3V_0$ and the magnitude is around 0.15, values very close to what has been deduced in experimental data for Au QP.

# 7   Conclusions

To conclude, a study of the features of multifragmenting sources formed in Xe+Sn mono-sources between 32 and 50 A MeV and Au QP at 80 A MeV has been reported. Scaling law of the cluster yields, ranking in the average size of fragment and fluctuations in cluster sizes and kinetic observables have been used to characterize the fragmentation process over a wide range of excitation energy.

From the analysis of cluster yields, we have shown that all data follow a Fisher scaling which coherently points to an excitation energy of $\simeq 4$ A MeV associated with a power law distribution. This "critical point" corresponds closely to the region of maximum fluctuations both of the configurational energy and the charge of the largest fragment. Theoretical models suggest that such point may not be associated with a critical behaviour, but also be characteristic of a subcritical behaviour (coexistence region of a first order phase transition). The high value of configurational energy fluctuations observed in our data set tends to confirm this interpretation. Data discussed in this work are compatible with a subcritical phenomenon. This interpretation of our results also agrees with previous analyses, on the same systems, about other signals of phase transition like spinodal decomposition and bimodality [29,32,33,34].

A Zipf-like analysis on the average cluster charge has been carried out and indicates that the Zipf law is observed at an excitation energy which does not coincide with the critical energy deduced from the other analyses. A coherent picture from various criticality signals and Zipf law is not observed neither for Xe+Sn mono-sources nor Au QP.

## References

[1]  P.J. Siemens, Nature (London) 305, 410 (1983)

[2]  "Dynamics and thermodynamics with nucleonic degrees of freedom", Ph. Chomaz, F. Gulminelli, W. Trautmann and S. Yennello (Eds.), in: Eur. Phys. J. A 30 (2006) #1 (a topical issue)

[3] B. Tamain, Eur. Phys. J. A 30 (2006) 71

[4] X. Campi and H. Krivine, Z. Phys. A 344 (1992) 81

[5] Y. G. Ma et al., Phys. Rev. Lett. 83 (1999) 3617

[6] Y. G. Ma, Eur. Phys. J. A 6 (1999) 367

[7] F. Gulminelli and P. Chomaz Phys. Rev. Lett. 82 (1999) 1402

[8] F. Gulminelli et al., Phys. Rev. C 65 (2002) 051601

[9] P. Chomaz and F. Gulminelli, Nucl. Phys. A 647 (1999) 153

[10] Ph. Chomaz, V. Duflot and F. Gulminelli, Phys. Rev. Lett 85 (2000) 3587

[11] M.E. Fisher, Physics, 3 (1967) 255

[12] Ph. Chomaz, Proc. of the Int. Nucl. Phys. Conf. INPC, "Nuclear Physics in the 21$^{st}$ century", Berkeley (USA), E. Norman, L. Schroeder, G. Wozniak (Eds.), in: American Institute of Physics conference proceedings, vol. 610 (2001) p. 167

[13] J.B. Elliott et al., Phys. Rev. Lett. 88 (2002) 042701

[14] J.B. Elliott et al., Phys. Rev. C 67 (2003) 024609

[15] L. Phair et al., Proc. of the XLth Int. Winter Meeting on Nucl. Phys., Bormio (Italy), I. Iori and A. Moroni (Eds.), in: Ricerca Scientifica ed Educazione Permanente, Suppl., vol. 119 (2002) p. 153

[16] M.K. Berkenbusch, W. Bauer et al., Phys. Rev. Lett. 88 (2002) 022701

[17] R.P. Scharenberg et al., Phys. Rev. C 64 (2001) 054602

[18] M. D'Agostino et al., Nucl. Phys. A 724 (2003) 455

[19] "Human Behaviour and the Principle of Least Effort", G.K Zipf, Addison-Wesley, Cambridge, (1949)

[20] M.S. Watanabe, Phys. Rev. E 53 (1996) 4187

[21] Y. G. Ma, R. Wada, K. Hagel et al., Phys. Rev. C 69 (2004) 031604

[22] Y. G. Ma, J. Natowitz et al., Phys. Rev. C 71 (2005) 054606

[23] X. Campi and H. Krivine, Phys. Rev. C 72 (2005) 057602

[24] M. D'Agostino et al., Phys. Lett. B 473 (2000) 219

[25] R. Bougault et al., Proc. of the XXXVIIIth Int. Winter Meeting on Nucl. Phys., Bormio (Italy), I. Iori and A. Moroni (Eds.), in: Ricerca Scientifica ed Educazione Permanente, Suppl., vol. 116 (2000) p. 404

[26] N. Le Neindre, Ph.D. thesis (1999), http://tel.ccsd.cnrs.fr/tel-00003741

[27] M. D'Agostino et al., Nucl. Phys. A 699 (2002) 795

[28] B. Borderie et al., Phys. Rev. Lett. 86 (2001) 3252

[29] G. Tăbăcaru et al., Eur. Phys. J. A 18 (2003) 103

[30] J. Pochodzalla et al., Phys. Rev. Lett. 75 (1995) 1040

[31] B. Borderie, J. Phys. G: Nucl. Part. Phys. 28 (2002) R217

[32] M. Pichon, Ph.D. thesis (2004), http://tel.ccsd.cnrs.fr/tel-00007451 and M. Pichon, B. Tamain et al., Nucl. Phys. A 779 (2006) 267

[33] M. Pichon et al., Nucl. Phys. A 749 (2005) 93

[34] E. Bonnet et al.,Proc. of the Int. Workshop on Multifragmentation and related topics, Catania, (Italy), R. Bougault, A. Pagano, S. Pirrone, M-F. Rivet and F. Rizzo (Eds.), (2005) 345

[35] M.F. Rivet et al., Phys. Lett. B 430 (1998) 217

[36] J. D. Frankland et al., Nucl. Phys. A 689 (2001) 940.

[37] G. Tăbăcaru et al., Nucl. Phys. A 764 (2006) 371.

[38] N. Le Neindre et al., Proc. of the XLth Int. Winter Meeting on Nucl. Phys., Bormio (Italy), I. Iori and A. Moroni (Eds.), in: Ricerca Scientifica ed Educazione Permanente, Suppl., vol. 119 (2002) p. 144

[39] N. Le Neindre et al., Proc. of the Int. Workshop on Multifragmentation and related topics, Catania, (Italy), R. Bougault, A. Pagano, S. Pirrone, M-F. Rivet and F. Rizzo (Eds.), (2005) 271

[40] M. F. Rivet et al., Nucl. Phys. A 749 (2005) 73

[41] J. Pouthas et al., Nucl. Instrum. Methods Phys. Res. A 357 (1995) 418

[42] J. Pouthas et al., Nucl. Instrum. Methods Phys. Res. A 369 (1996) 222

[43] J. Lukasik, et al., Phys. Rev. C 66 (2002) 064606

[44] A. Trzcinski et al., Nucl. Instrum. Methods Phys. Res. A 501(2003) 367

[45] J. D. Frankland et al., Nucl. Phys. A 689 (2001) 905.

[46] E. Bonnet et al., in preparation

[47] E. Bonnet, Ph.D. thesis (2006), http://tel.ccsd.cnrs.fr/tel-00121736

[48] M. D'Agostino et al., Nucl. Phys. A 650 (1999) 329

[49] P. Mastinu et al., Phys. Rev. Lett. 76 (1996) 2646

[50] J. D. Frankland et al., Phys. Rev. C 71 (2005) 034607.

[51] V.E. Viola and R. Bougault, Eur. Phys. J. A 30 (2006) 215

[52] T. Kubo et al., Zeitschrift für Physik A 352, n⁰2 (1995) 145

[53] P. Finocchiaro et al., Nucl. Phys. A 600 (1996) 236

[54] F. Gulminelli et al., Proc. of the XLth Int. Winter Meeting on Nucl. Phys., Bormio (Italy), I. Iori and A. Moroni (Eds.), in: Ricerca Scientifica ed Educazione Permanente, Suppl., vol. 119 (2002) p. 128

[55] F. Gulminelli Ann. Phys. Fr.29 n$^o$6 (2004)

[56] F. Gulminelli, P. Chomaz Phys. Rev. C 71 (2005) 054607

[57] D.H.E. Gross, Microcanonical Thermodynamics: Phase Transitions in Finite Systems, Lecture Notes in Physics, vol. 66, World Scientific, Singapore, (2001)

[58] M. D'Agostino et al., Nucl. Phys. A 734 (2004) 512

[59] M. Hasenbusch, K. Pinn and S. Vinti, hep-lat/9806012

[60] D. Stauffer and A. Aharony, Percolation Theory, 2nd ed., Taylor and Francis, (1995)

[61] A. Bonasera et al., "La Rivista del Nuovo Cimento" (2000) vol.23 n$^o$2

[62] W. Bauer, S. Pratt, B. Alleman, Heavy Ion Physics, in print (2006); W. Bauer, Proc. of the Int. Workshop on Multifragmentation and related topics, Catania, (Italy), R. Bougault, A. Pagano, S. Pirrone, M-F. Rivet and F. Rizzo (Eds.), (2005) 279

[63] J Kertész Physica 161 (1989) 58

[64] X. Campi, H. Krivine, A. Puente, Physica A 262 (1999) 328

[65] J.P Bondorf, A.S Botvina, A.S Iljinov and I.N. Mishustin, Phys. Rep. 257 (1995) 133

[66] J.P Bondorf, A.S Botvina and I.N. Mishustin, Phys. Rev. C 58 (1998) R27

[67] P. Désesquelles et al., Nucl. Phys. A 633 (1998) 547